Trailing edge subcomponent testing for wind turbine blades–Part A: Comparison of concepts

Rosemeier, M.; Antoniou, Alexandros ; Chen, Xiao; Lahuerta, F.; Berring, Peter; Branner, Kim

Published in:
Wind Energy

Link to article, DOI:
10.1002/we.2301

Publication date:
2019

Document Version
Publisher's PDF, also known as Version of record

Citation (APA):
Rosemeier, M., Antoniou, A., Chen, X., Lahuerta, F., Berring, P., & Branner, K. (2019). Trailing edge subcomponent testing for wind turbine blades–Part A: Comparison of concepts. Wind Energy, 22(4), 487-498. https://doi.org/10.1002/we.2301

Received: 17 April 2018 | Revised: 16 August 2018 | Accepted: 3 November 2018
DOI: 10.1002/we.2301

WILEY

RESEARCH ARTICLE

Trailing edge subcomponent testing for wind turbine blades–Part A: Comparison of concepts

M. Rosemeier[1] | A. Antoniou[1] | X. Chen[2] | F. Lahuerta[3] | P. Berring[2] | K. Branner[2]

[1]Department of Rotor Blades, Fraunhofer IWES, Fraunhofer Institute for Wind Energy Systems, Bremerhaven, Germany
[2]Department of Wind Energy, Technical University of Denmark, Roskilde, Denmark
[3]Knowledge Centre WMC, Wieringerwerf, The Netherlands

Correspondence
M. Rosemeier, Department of Rotor Blades, Fraunhofer IWES, Fraunhofer Institute for Wind Energy Systems, Am Seedeich 45, Bremerhaven 27572, Germany.
Email: malo.rosemeier@iwes.fraunhofer.de

Funding information
FP7 Energy, Grant/Award Number: 609795

Abstract

As a complement to the mandatory structural full-scale test for wind turbine blades, the method of subcomponent testing has recently been proposed by international standards and guidelines for the experimental investigation of design-critical full-scale parts. This work investigated different subcomponent test (SCT) concepts for a trailing edge of an outboard segment from a 34-m blade. Detailed analytical models to design the SCT concepts with regard to the boundary conditions were derived. Finite element analyses of the SCT's linear response were benchmarked against each other and against the full blade model in terms of displacements, rotations, in-plane strains, and energy consumption. All SCT concepts were in good agreement with the full-scale test with respect to the longitudinal strain response but showed deviations in the transverse and shear strain, as well as in the rotational and displacement response.

KEYWORDS

blade design, certification, composite structure, full-scale blade testing, model verification, structural testing

1 | INTRODUCTION

Recent years have witnessed remarkable progress in wind energy technology. In particular, rotor blades have become longer and more slender to capture more power from the wind while reducing the loads on the turbine. Developing a new type of large rotor blade is a challenging task. Detailed design, high-quality manufacturing, and rigorous testing are required before the prototype can be mass produced. One of the key elements in this development process is the full-scale structural testing required for the certification of the blade type.[1,2] The purpose of the tests is to confirm to an acceptable level of probability that the whole population of a blade type fulfills the design assumptions.[1] Owing to the high cost of both the specimen and the test, only one prototype blade is typically tested at full scale in the following sequence: under static load, fatigue load, and post-fatigue static load. This testing method has been widely used to certify a new blade design.

Some major concerns still exist regarding the current full-scale testing method:

- The limited coverage of realistic loading conditions. The basis for establishing the test loads is the entire envelope of blade design loads. The full-scale testing does not necessarily cover all critical loading conditions along the blade length as they would occur in the field,[3] for example, in a trailing edge bond line under combined flap-wise and lead-lag loading. Moreover, some transient loads such as impact during transportation and installation cannot be simulated in the full-scale test, but they may cause local damage in the blade. More suitable test methods and setups are required to examine these critical loading conditions.
- The large effort associated with correcting problems. The development procedure of a new blade type follows a path from design through manufacturing to testing. The effort of correcting design problems increases significantly with each phase in the blade development. Although

Abbreviations: AM, analytical model; BJ, ball joint; BJ-SCT, ball joint SCT concept; CF-SCT, C-frame SCT concept; FEM, finite element model; FST, full-scale blade test; LTT, leading-to-trailing edge load case; SC, subcomponent; SCT, subcomponent test.

it is possible to identify design problems during the testing program, a method that allows problem detection earlier in the design phase can reduce the uncertainty in the blade development.

- The lack of representativeness. Testing one or two prototypes does not provide a statistical distribution of the structural performance of the whole population of blades. In particular, the blade used for the certification test is usually one of the first blades from series production, which is still subject to developmental modifications. How the performance of the prototype blade represents other blades is still unclear. More tests are necessary to obtain statistically meaningful results to increase structural reliability.

Solutions to overcome the above shortcomings of certification tests are not straightforward, especially taking into account practical constraints stemming from technical and economic aspects. One possible way of improving the current design process is to use a subcomponent test (SCT). A subcomponent (SC) is considered to be a structural part cut directly out of a wind turbine rotor blade[4]; it therefore corresponds to the full blade's scale. The approach is to test blade SCs using specific test methods and in particular test setups to complement the full-scale testing.

Several studies focusing on an SCT of blade segments have been carried out.[5-8] Recently, Branner et al,[9] Lahuerta et al,[10] and Rosemeier et al[11] have proposed SCTs for segments of 3-m length to investigate the structural performance of trailing edge bond lines in particular. This study focuses on these three SCT concepts and compares them with each other.

The successful implementation of an SCT into the certification process[2] of a blade prototype still faces several challenges. To reproduce the more realistic loading conditions experienced by the full-scale blade, special attention should be paid to the questions: How different loads are transferred in the SCs and how an SCT can generate the same structural responses, such as deformation, load-carrying capacity, and failure modes, which are expected in the blade during the full-scale testing? To answer these questions, specific test methods are developed in this work for the test specimens and test setups. Ideally, specimens used in an SCT should represent the actual geometry and materials of the blade regions that are potentially critical. One solution would be cutting the SCs from the blades or manufacturing them from the blade molds. Nevertheless, the sampling locations and the sizes of the SCs to be tested still need more study. Moreover, one of the essential differences between SCs and their parent structures are the boundary conditions. It is difficult to fully reproduce the boundary conditions in an SCT as the SCs are clamped or simply supported in the test rig and the deformation at the blade segment edges is therefore constrained. Specific test setups should be developed to reduce the effects of artificial boundary conditions.

Lead-lag fatigue loading is driving the design of today's and future rotor blades.[12] Therefore, this work focuses on the most sensitive area for the lead-lag load case, ie, on the trailing edge bond line in particular. Also, current research is also focusing on rotor blade trailing edge failures. [13-16]

An outboard segment of the SSP34 blade[17] was chosen as the use case for this study. The blade underwent several research tests focusing on the ultimate static response, ie, its failure at the trailing edge, for example.[16]

Specific objectives of this paper are to compare different test concepts for trailing edge SCs with each other and to compare the concepts with the full-scale test.

The paper is structured as follows: Section 2 introduces the SCT concepts considered. Section 3 presents analytical and finite element (FE) models. Section 4 summarizes the comparison between the different concepts replicating the response of the full-scale test.

2 | STRUCTURAL TEST CONCEPTS

2.1 | Static full-scale blade test

One of the goals of this work is to mimic the traditional static full-scale blade test by means of an SCT. Therefore, the load and strain conditions in a full-scale test are explained.

The leading-to-trailing edge (LTT) load direction where the trailing edge is under compression was selected as the benchmark load case (Figure 1A). The target bending moment distribution of the full-scale test in the lead-lag direction is achieved via shear forces F_i, leading to a multilinear test bending moment distribution. The loading condition at cross-sectional level depends on the angle θ between load axis and elastic axis (Figure 1B) resulting in a combination of edge-wise and flat-wise bending. Thus, the neutral axis is angled with respect to the yz_R-plane of the reference coordinate system. The axial strain distribution can be idealized as a linear distribution about the axis perpendicular to the neutral axis. In an SCT, it is essential to find a setup that replicates this strain distribution.

2.2 | Subcomponent test concepts

Two basic SCT concepts are compared in this work. Both are explained in the following sections.

2.2.1 | C-frame concept

A C-frame (CF)-SCT full wherein a blade segment with a full cross section is mounted in a test rig with two load frames (similar to full-scale frames) and hinged beams that are connected to an actuator (Figure 2A). Alternatively, to reduce the test loads required, the cross section is cut in the span-wise direction (CF-SCT concept) such that only the area of interest remains, in this case the trailing edge cell including one main shear

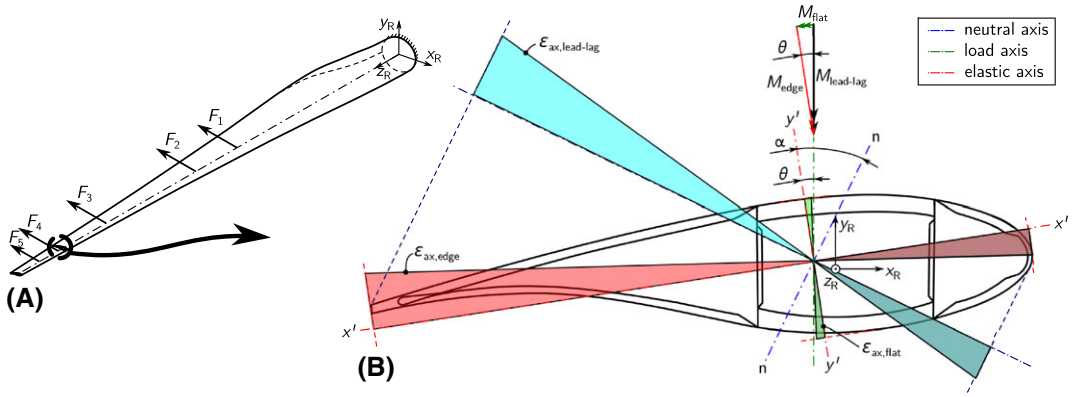

FIGURE 1 Shear forces F_i applied in the static lead-lag leading-to-trailing-edge full-scale certification blade test A. A representative cross section in the outboard blade region is extracted to show the local cross-sectional loading conditions B. The internal bending moment is split into a flat-wise and an edge-wise component. The superposition of the axial strains $\varepsilon_{ax,edge}$ and $\varepsilon_{ax,flat}$ result in a lead-lag strain $\varepsilon_{ax,lead\text{-}lag}$ [Colour figure can be viewed at wileyonlinelibrary.com]

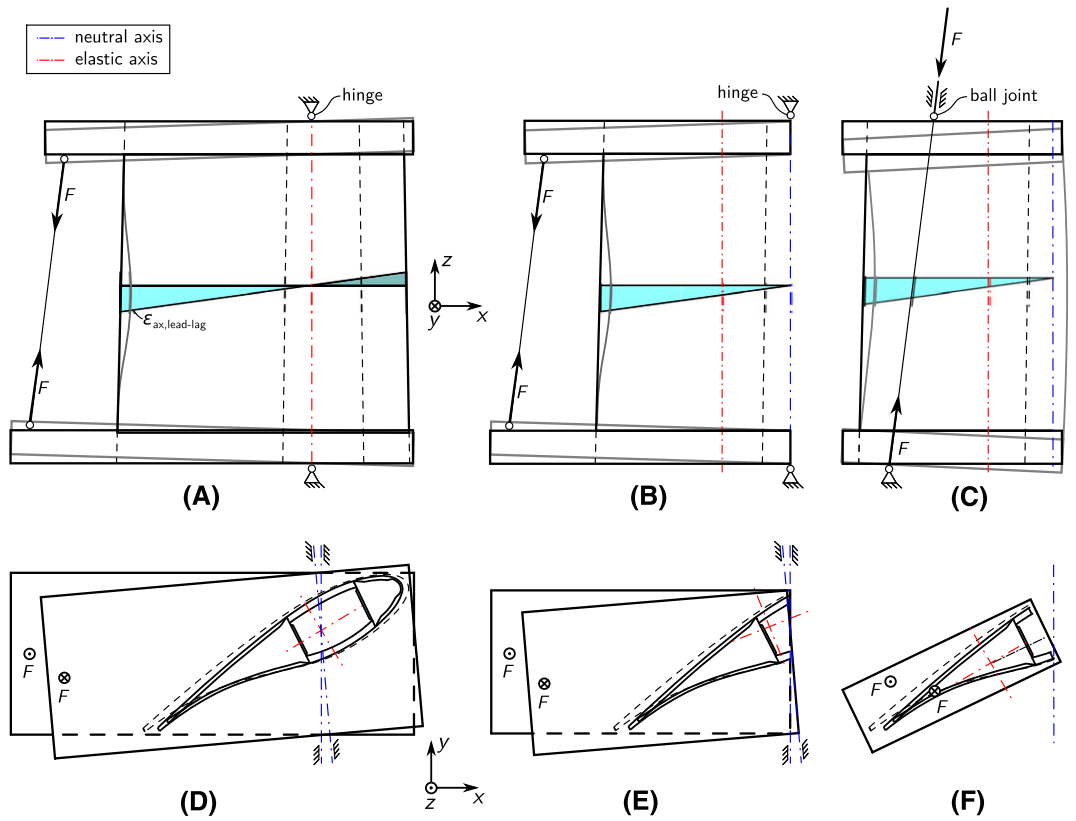

FIGURE 2 Side views of the replacement models for the trailing edge subcomponent testing concepts: full cross-section in hinged C-frame subcomponent test A, cut cross-section in hinged C-frame subcomponent test B, and cut cross section simply supported by ball joints subcomponent test C. Top views of the respective side views D, E, and F. The deformed shape is shown in gray [Colour figure can be viewed at wileyonlinelibrary.com]

web (Figure 2B). The hinges are positioned along the neutral axis *n* of the full blade cross section. The two hinges can be rotated arbitrarily about the z_R-axis to introduce any load combination of lead-lag and flap-wise loading. Also, the cantilever arms creating the bending moments at both edges can be chosen arbitrarily to define a bending moment distribution.

2.2.2 | Ball joint concept

A blade segment is mounted in a simply supported test rig (ball joint [BJ]-SCT) with two load frames connected to two BJs (Figure 2C). An eccentric axial load is introduced at one joint, thereby introducing a normal force superposed by a bending moment. The position of the two joints within the cross-sectional plane can be chosen arbitrarily, which enhances the introduction of any load combination and the distribution of lead-lag and flap-wise loading.

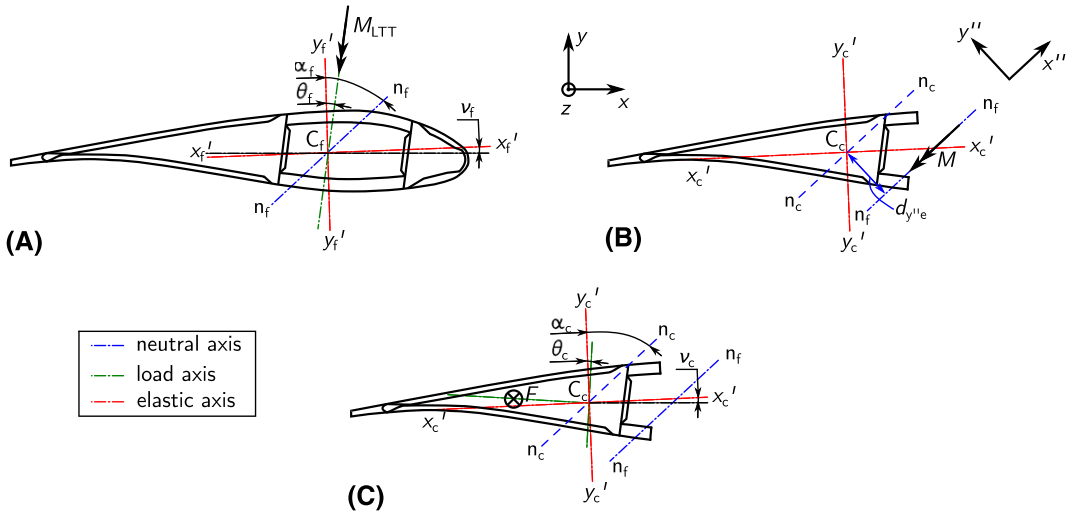

FIGURE 3 Inclination angles, load vectors, elastic, and neutral axes of full cross section in full-scale blade test A, cut cross section in C-frame subcomponent test concept B, and in ball joints subcomponent test concept C [Colour figure can be viewed at wileyonlinelibrary.com]

3 | METHODS

3.1 | Analytical cross-sectional models

The blade cross sections were modeled on the basis of Euler–Bernoulli beam theory.[18] The analytical cross-sectional models (AMs) were used to investigate the effect of the boundary conditions on the structural performance of several SCT concepts. To this end, the cross-sectional properties, ie, axial and bending stiffnesses, location of the elastic center (also called centroid), the structural twist of the full blade cross section, and the cut cross section were determined using the Beam Cross Section Analysis Software (BECAS).[19-22] The blade parametrization and input generation was conducted using workflows based on the FUSED-Wind framework,[23] allowing the fast generation and analysis of full and cut cross-sectional models.

To enhance the comparison between FST and SCT, the strain distribution along the cross sections was modeled with respect to the cross-sectional elastic and neutral axes.

3.1.1 | Full-scale test model

Given the cross-sectional properties of the full blade and the full-scale test (FST) load case direction vector at the target cross section, the longitudinal strain perpendicular to the blade cross-sectional plane can be determined within the coordinate system of the elastic axes:

$$\varepsilon_{z\mathrm{FST}}\left(x'_{\mathrm{f}}, y'_{\mathrm{f}}\right) = \frac{M_{x'\mathrm{FST}}}{E_{\mathrm{f}} I_{x'\mathrm{f}}} y' + \frac{M_{y'\mathrm{FST}}}{E_{\mathrm{f}} I_{y'\mathrm{f}}} x', \tag{1}$$

where $M_{x'\mathrm{FST}}$ and $M_{y'\mathrm{FST}}$ represent the bending moment transformed from the blade root coordinate system (Figure 3A) into the coordinate system of the elastic axes x'_{f}, y'_{f} of the full cross section. $E_{\mathrm{f}} I_{x'\mathrm{f}}$ and $E_{\mathrm{f}} I_{y'\mathrm{f}}$ denote the bending stiffnesses about the elastic axes.

The inclination angle* α_{f} between the elastic y'_{f}-axis and the neutral axis n_{f} (Figure 3A) can be determined using the relation[24]:

$$\alpha_{\mathrm{f}} = \arctan\left(\frac{I_{y'\mathrm{f}}}{I_{x'\mathrm{f}}} \cdot \tan\theta_{\mathrm{f}}\right), \tag{2}$$

where θ_{f} denotes the inclination angle between the elastic y'_{f} and the load axis of the local bending moment vector M_{LTT} in an FST. The angle between the neutral axis n_{f} and the reference y-axis (cross section coordinate system as shown in Figure 3) is defined as follows:

$$\gamma_{\mathrm{f}} = \alpha_{\mathrm{f}} + \nu_{\mathrm{f}}, \tag{3}$$

where ν_{f} is defined as the angle between the reference x-axis and the elastic x'-axis.

3.1.2 | C-frame subcomponent test model

For the CF-SCT, the cross-sectional area is trimmed to the area of interest (Figure 3C). The aim is to subject the cut cross section to the same strain distribution as in the full-scale blade test (Equation 1). Therefore, the required inclination angle of the load axis θ_{c} is determined with

*Angles are defined as being positive when they lie between the first and second axes in the sequence mentioned, eg, α_{f} is negative when the constellation of the y'_{f}-axis and the neutral axis n_{f} is as shown in Figure 3A.

Equation 2 aiming for a neutral axis n_c and an inclination α_c parallel to the neutral axis of the full cross section n_f:

$$\theta_c = \arctan\left(\frac{I_{x'c}}{I_{y'c}} \cdot \tan\alpha_c\right), \tag{4}$$

where α_c is determined using the following:

$$\alpha_c = \gamma_f - \nu_c, \tag{5}$$

where ν_c is the angle between the reference x-axis and the elastic x'_c-axis of the cut cross section.

Now, the area moment of inertia about the neutral axis of the full cross section is calculated using the following[24]:

$$I_{x''c} = \frac{I_{x'c} + I_{y'c}}{2} + \frac{I_{x'c} - I_{y'c}}{2} \cdot \cos 2\alpha_c + A_c\, d^2_{y''e}, \tag{6}$$

where $d_{y''e}$ denotes the distance between the elastic center of the full and the cut cross-section within the hinge $x''y''$-coordinate system (Figure 3C). A_c denotes the area of the cut cross section.

The longitudinal strain along the blade cross section surface coordinates (x''_c, y''_c) can be determined using the following:

$$\varepsilon_{zCF\text{-}SCT}(x''_c, y''_c) = \frac{M}{E_c I_{x''c}} y''_c. \tag{7}$$

Given the target strain distribution at the specimen's trailing edge ε_{zTE}, the required moment M can be found by rearranging Equation 7:

$$M = \frac{\varepsilon_{zTE}\, E_c I_{x''c}}{y''_{cTE}}. \tag{8}$$

Given the optimum bending moment M for each cross-section along the specimen, the cantilever arm length, the hinge position, and the hinge rotation angle at the specimen edges are used as design variables to optimize the strain field of the specimen with respect to the target FST load case.

If the specimen is not cut and remains as a full cross section, α_f is determined from Equation 2. Using the area moments of inertia of the full cross section, Equation 6 can be reduced by the stiffness fraction because of the parallel axis theorem:

$$I_{x''f} = \frac{I_{x'f} + I_{y'f}}{2} + \frac{I_{x'f} - I_{y'f}}{2} \cdot \cos 2\alpha_f \tag{9}$$

Equations 7 and 8 are then applied analogously replacing index c by index f.

3.1.3 | Ball joint subcomponent test model

For the BJ-SCT concept, the cross section area is trimmed to the area of interest as in the CF-SCT concept (Figure 3C). The aim, as also described in the previous section, is to subject the cut cross section to the same strain distribution as in the FST. Therefore, the angle θ_c is determined using Equation 4. The longitudinal strain along the blade cross section surface coordinates can be determined by superposing axial contraction and bending due to eccentric load introduction using the following:

$$\varepsilon_{zBJ\text{-}SCT}(x'_c, y'_c) = \frac{F}{A_c E_c} + \frac{F\, I_{y'cF}}{E_c I_{x'c}} y' + \frac{F\, I_{x'cF}}{E_c I_{y'c}} x'. \tag{10}$$

The load F introduced eccentrically at the load introduction point $(I_{x'cF}, I_{y'cF})$ generates a bending moment about the neutral axis n_c. Thus, the cantilever arm for introducing load F is perpendicular to θ_c (Figure 3C):

$$\cot\theta_c = \frac{I_{y'f}}{I_{x'f}}. \tag{11}$$

The load introduction point is determined using Equation 11 and by setting Equation 10 equal to 0 for the strain in the elastic center of the full cross section (x'_{ef}, y'_{ef}):

$$I_{x'f} = -\frac{I_{x'c}\, I_{y'c}}{A_c\left(\cot\theta_c\, I_{y'c}\, y'_{ef} + I_{x'c}\, x'_{ef}\right)}. \tag{12}$$

Given the target strain distribution at the specimen's trailing edge ε_{zTE}, the required force F can be found by rearranging Equation 10:

$$F = \frac{A_c E_c\, I_{x'c}\, I_{y'c}\, \varepsilon_{zTE}}{A_c\left(x'_{cTE}\, I_{x'f}\, I_{x'c} + I_{y'c}\, y'_{cTE}\, I_{y'f}\right) + I_{x'c}\, I_{y'c}}. \tag{13}$$

Subsequently, F, $I_{x'f}$ and $I_{y'f}$ can be calculated for each cross-section along the specimen. This results in the corresponding bending moment distributions

$$M_x(z) = F(z) \cdot I_{x'f}(z) \quad \text{and } M_y(z) = F(z) \cdot I_{y'f}(z). \tag{14}$$

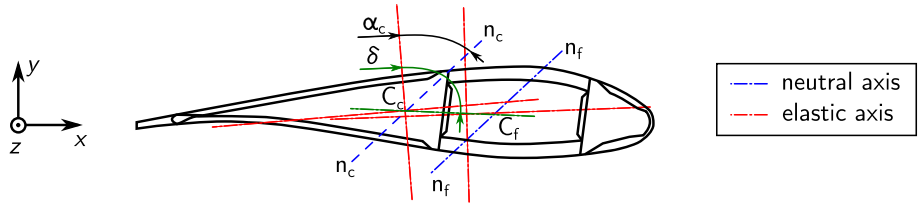

FIGURE 4 Axis through the centroids of full and cut cross section [Colour figure can be viewed at wileyonlinelibrary.com]

Since only a constant force can be applied along the specimen, the optimum load F_{appl} is applied, which induces the cross-sectional strain in the target area plus the desired strain along the trailing edge. Furthermore, there are only two positions at the two specimen edges where the load introduction points can be positioned. Therefore, the bending moment distributions are divided by F_{appl} to determine the length of the cantilever arms required to produce the constant force applied at each cross section:

$$l_{x'Fappl}(z) = \frac{M_y(z)}{F_{appl}} \quad \text{and} \quad l_{y'Fappl}(z) = \frac{M_x(z)}{F_{appl}}. \tag{15}$$

A best fit axis through the points $\left(l_{x'Fappl}, l_{y'Fappl}\right)$ is derived along the specimen, which can be used to determine the BJ positions at root and tip end.

Alternatively, the optimum load introduction point with a constant force can be found by using Equation 11 and rearranging Equation 10:

$$l_{x'Fappl} = -\frac{l_{x'c}\, l_{y'c}\,(F - A_c E_c\, \varepsilon_{zTE})}{F\, A_c\left(l_{x'c}\, x'_{cTE} + l_{y'c} \cot\theta_c\, y'_{cTE}\right)} \tag{16}$$

A theoretical limit exists for the applicable load direction. The limit is reached when the neutral axes n_c and n_f are congruent (Figure 4), or in other words if the inclination angle α_c is within the range between

$$\delta < \alpha_c < \delta + 180°, \tag{17}$$

where

$$\delta = 90° + \gamma_f + \tan\left(\frac{y_{Cf} - y_{Cc}}{x_{Cf} - x_{Cc}}\right). \tag{18}$$

Using Equations 2 to 5 the inclination angle of the load axis limits can be determined:

$$\theta_f = \arctan\left(\frac{l_{x'f}}{l_{y'f}} \cdot \tan\left(\arctan\left(\frac{l_{y'c}}{l_{x'c}} \cdot \tan\theta_c\right) + \nu_c - \nu_f\right)\right). \tag{19}$$

3.2 | Finite element models

A 3D full blade finite element model (FEM) with 119 499 shell and 2900 solid elements (362 705 nodes) was generated in the FE Mechanical Analysis System Parametric Design Language (MAPDL)[25] based on the SSP34 blade laminate plan and geometry[26] (Figure 5). The model has been verified with two existing FE models of other software packages,[16,27] and validated with full-scale experiments.[28] Furthermore, three FE models representing the SCT concepts were generated (Figure 6): A model of the full cross section in the CF-SCT with 8284 shell and 288 solid elements (25 524 nodes), and models of the cut cross section in the CF-SCT and BJ-SCT with 5238 shell and 288 solid elements (16 588 nodes).

3.2.1 | Model layout

The FE models were assembled with eight-noded quadratic shell elements of type SHELL281. The trailing edge bond line was modeled using 20-noded quadratic solid elements of type SOLID186, which share their nodes with the shell elements at the interfaces. This technique is commonly used in the modeling of wind turbine blades.[7,29] Other approaches using shell-solid modeling with kinematic couplings were investigated by Haselbach.[30]

The full blade model was subjected to the LTT certification load case according to IEC[1] via five shear forces representing ropes that were connected to a strong wall. The ropes were implemented as LINK11 type elements. The ends of the rope were simply supported on the wall and on a master node on the blade's pitch axis, respectively. The latter was connected to the blade structure through multipoint constraint elements of type RBE3.

For the SCT models a specimen length of 2.75 m was chosen, since it represented the length of the available specimens of the 34-m blade investigated for future experimental validation.

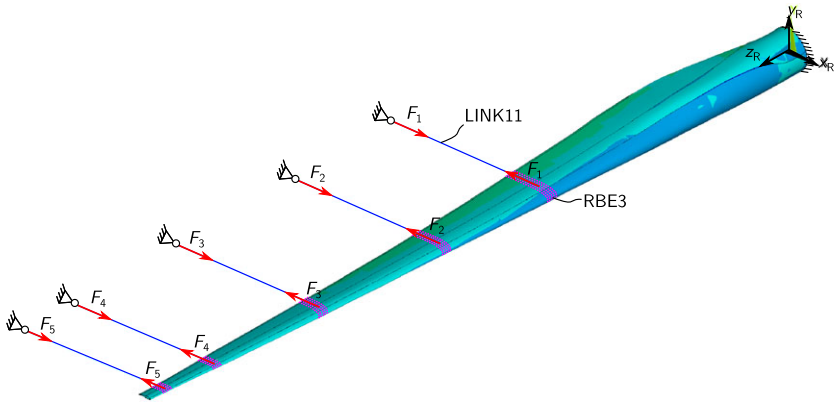

FIGURE 5 Deformed finite element model of the full blade model and boundary conditions of leading-to-trailing edge load case. The color scale shows the longitudinal strain ε_{zR} [Colour figure can be viewed at wileyonlinelibrary.com]

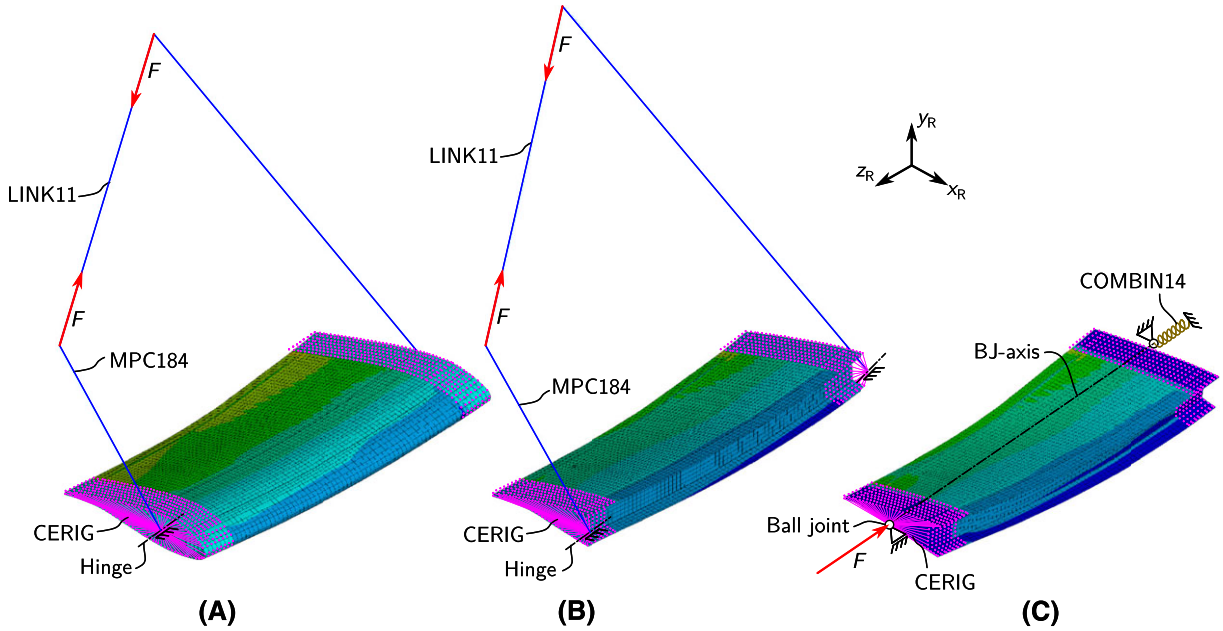

FIGURE 6 Deformed finite element models of the full cross-section within C-frame subcomponent test A, and cut cross section within C-frame subcomponent test B, and ball joint subcomponent test C. The boundary conditions are shown for the replication of the full-scale leading-to-trailing edge load case. The color scale shows the longitudinal strain ε_{zR} [Colour figure can be viewed at wileyonlinelibrary.com]

In the C-frame models the edges of the SC were clamped with CERIG type rigid elements representing the load frame. A load frame width of 30 cm was chosen to ensure a potentially glued connection had reasonable integrity. A master node was positioned at the hinge axis, which represents the rotational degree of freedom of the load frame. Rigid beams of type MPC184 were dimensioned in length such that they introduce the required bending moments at the root and tip frame. An actuator (LINK11) was positioned between the two beams.

For the model of the BJ concept, the two master nodes of the CERIG elements representing the BJs were positioned at the root and tip ends. A torsional spring of type COMBIN14 was connected to the BJ at the root end so as to be congruent to the axis through both BJs (BJ-axis). The torsion spring constant was chosen to be as flexible as required such that the rigid body motion along the BJ-axis was suppressed, in this case $c = 1 \cdot 10^{-3}$ N m rad^{-1}. While the BJ displacements at the root end were fully constrained, BJ displacement at the tip end was allowed along the BJ-axis.

3.2.2 | Determination of boundary conditions

The SC structure under investigation was cut out of the full blade FEM. The SC was then sliced into 25 cross sections whose properties were determined by BECAS. This was also done for 41 cross sections of the full blade. The boundary conditions at the tip and root frame, ie, the hinge positions and angles, and the bending moments required for the CF-SCT, and the BJ positions for the BJ-SCT, were determined using the analytical full and cross sectional models of the SCTs as described in section 3.1. These boundaries were applied in the respective FE model as shown in Figure 6. All FE simulations were conducted as a linear static analysis.

3.3 | Actuator work

The actuator work required for the static loading in the SCT concepts is determined by evaluating the strain energy that the actuator introduces into the specimen.[24] Assuming linearly elastic material behavior and a rigid connection between the actuator and the SC specimen, the actuator work is calculated as follows:

$$W_{\mathrm{BJ}} = \int_0^{\delta} F \, \mathrm{d}\delta = \frac{1}{2} F \delta, \tag{20}$$

where F denotes the external loading in terms of forces and δ denotes the displacement of the actuator (CF-SCT) or specimen (BJ-SCT). For the CF-SCT concept, the work can alternatively be calculated as follows:

$$W_{\mathrm{CF}} = \int_0^{\theta} M \, \mathrm{d}\theta = \frac{1}{2} \left(M_{\mathrm{r}} \theta_{\mathrm{r}} + M_{\mathrm{t}} \theta_{\mathrm{t}} \right), \tag{21}$$

where the external loading in terms of the bending moments at the root and tip hinge of the specimen edge is denoted by M_{r} and M_{t}, and the rotations by θ_{r} and θ_{t}, respectively.

4 | RESULTS AND DISCUSSION

4.1 | Replication of full-scale test response

4.1.1 | Displacement response

The overall deformation and rotation of the trailing edge (at $s = 0.0$ as shown in Figure 9A) is used as an indicator to compare the performance of the SCT with the FST; see Figure 7A-C. For comparative reasons the displacements and rotations of the specimen in all SCT concepts and the FST are transformed into the same coordinate system at the root end of the specimen. The coordinate system for the span-wise position z_{R} and

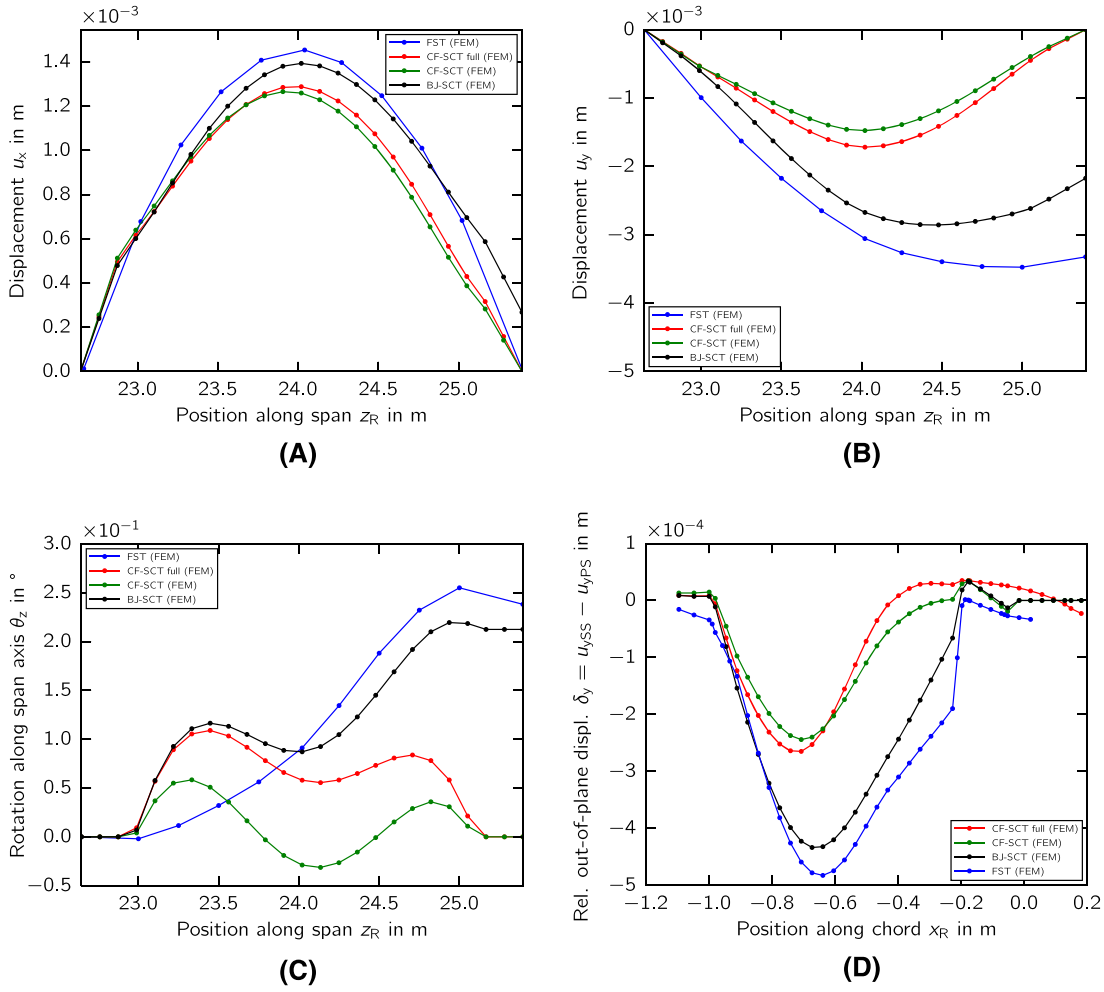

FIGURE 7 Trailing edge displacements along the span of full blade and subcomponent in the x_{R}-direction A, and y_{R}-direction B. Trailing edge rotations along the span are shown in C. The relative out-of-plane displacements in the y_{R}-direction between suction and pressure side at the target cross section are shown in D. Displacements and rotations were post-processed on the pressure side at $s = 0.0$ as shown in Figure 9A [Colour figure can be viewed at wileyonlinelibrary.com]

the chord-wise position x_R is illustrated in Figure 1. Moreover, the relative displacement δ_y between suction and pressure side panel along the chord of the target cross section in the middle of the specimen, ie, at a blade length of 24 m, is shown (Figure 7D).

The BJ-SCT displacement response is in good agreement with the FST, clearly followed by the CF-SCT with full and cut cross section, which are close to each other. In the latter two concepts, the rotation of the specimen is constrained at both edges. Therefore, the out-of-plane displacement u_y (Figure 7B) and rotation about the span θ_z (Figure 7C) are both zero at the tip end. In the BJ-SCT concept, in contrast, this rotation at the tip end is free. All SCT concepts show a wavy distribution of θ_z, which indicates a varying torsional moment along the specimen. The suction and pressure side panels approach each other in all simulations, meaning that the trailing edge cell is closing. The BJ-SCT is in better agreement with FST since it can freely rotate at both ends. This rotational degree of freedom has a substantial impact on the out-of-plane displacement, too.

4.1.2 | Strain response along trailing edge

Besides the displacement response, the longitudinal strain ε_z and shear strain γ_{zs} along the trailing edge (at $s = 0.0$ as shown in Figure 9A) are used as comparison parameters, see Figure 8A,B. The coordinate system of the shear strain is shown in Figure 9A.

The longitudinal strain distribution of all SCT concepts follows the slope of the strain distribution from FST simulations. At the edges, strain peaks are observed, which are a consequence of the constraints of the load frames. The match of the strain shape along the span depends on the fitting procedure of the longitudinal strain, as described in section 3.1. For the concepts using a cut cross section, the shape of the strain slope can be influenced by the span-wise cutting. To fully reproduce the strain distribution along the blade length, the position of the elastic center of the cut cross sections along the span needs to be tailored with respect to the elastic center of the full cross section.

The shear strain shows a wavy distribution as also observed in the rotation response (Figure 7C). Towards the tip region the shear strain of the BJ-SCT is close to the FST.

4.1.3 | Strain response at target cross section

The longitudinal strain ε_z, transverse strain ε_s and shear strain γ_{zs} along the surface coordinate of the target cross section are used as an indicator to compare the performance of an SCT with the FST; see Figure 9A,C, and E. The respective strain deviations of the SCT FE models and the analytical model with respect to the FST are highlighted in Figure 9B,D, and F.

All SCT concepts reproduce the FST longitudinal strain response at the trailing edge ($s = 0.0$ and $s = 1.0$) with reasonable accuracy, as already indicated in Figure 8A. When considering longitudinal strains along the suction and pressure side panels, the results of the CF-SCT concept with full cross section are in closest agreement with those of the FST with a maximum deviation of -3% to -4%. In the same case, the BJ-SCT concept deviates by -5% to -6%. When considering transverse and shear strains along the suction and pressure side panels, the CF-SCT concept with the full cross section shows the closest agreement to the FST. Comparing the shear strain response along the suction side ($s = 0.05 \ldots 0.33$) and pressure side panels ($s = 0.71 \ldots 0.95$), the deviations are larger on the suction side for the SCT concepts with cut cross section, ie, up to 50% on the PS and up to 260% on the SS for the BJ-SCT concept.

4.2 | Actuator response

The external loads F and M, as well as the displacement δ and the rotation angle θ were extracted from the SCT FE models (Table 1). The actuator work W was determined using Equations 20 and 21.

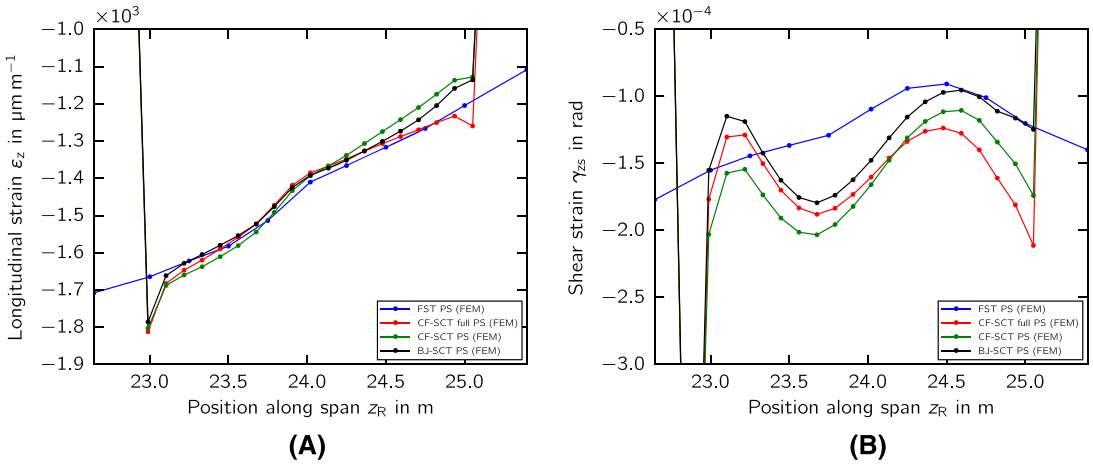

FIGURE 8 Longitudinal strain A, and shear strain B, at the trailing edge along the blade span. The strains were post-processed on the pressure side at $s = 0.0$ as shown in Figure 9A [Colour figure can be viewed at wileyonlinelibrary.com]

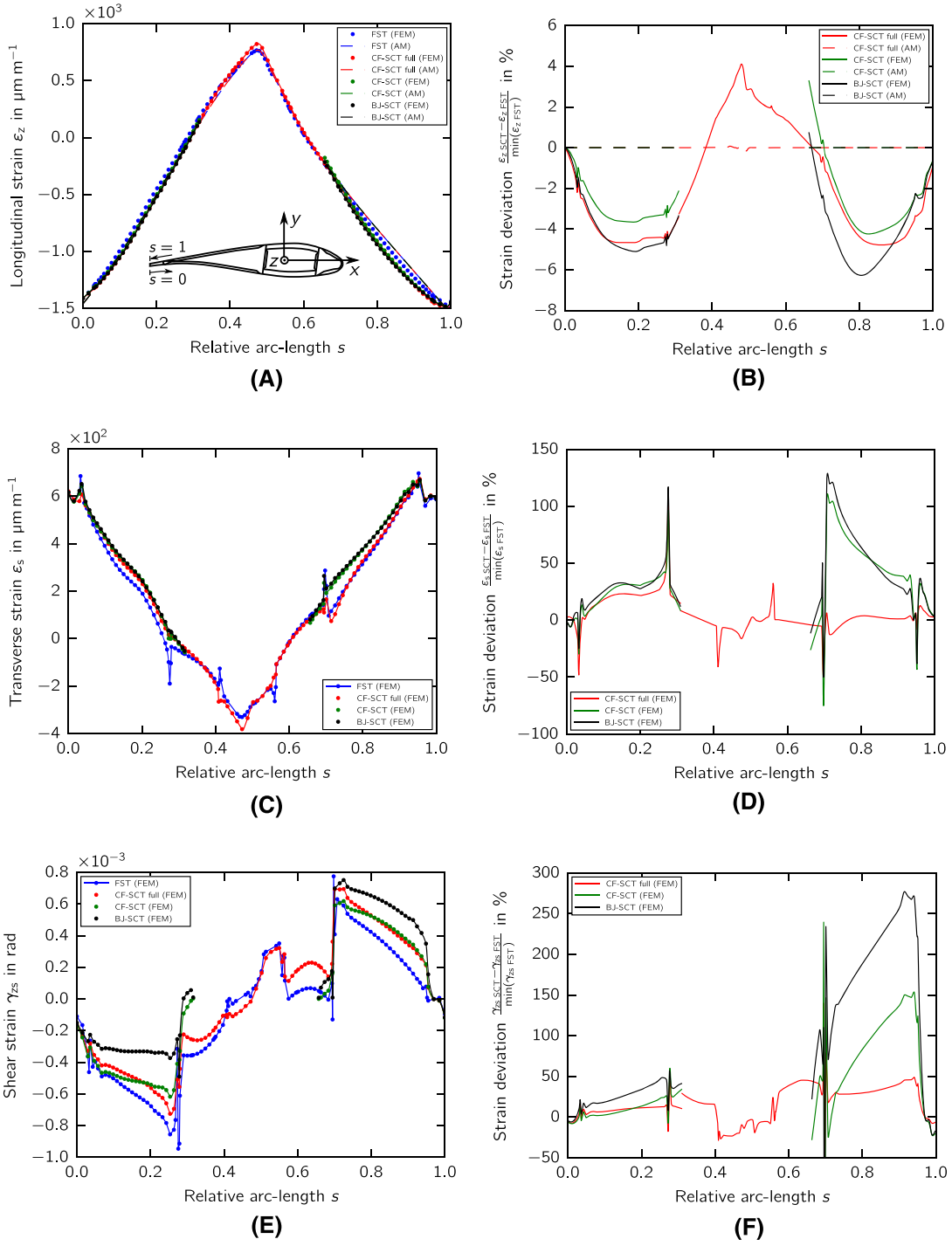

FIGURE 9 Longitudinal strain on the blade surface for a lead-lag full-scale blade test (FST) and its replication by subcomponent test (SCT) concepts A, and the relative deviation with respect to the lead-lag FST in B. The transverse strain is shown in C, and its relative deviation with respect to the FST in D. The shear strain is shown in E, and its relative deviation with respect to the FST in F. The strain is determined at the target cross section (24 m) at 100 % LTT test load with the analytical model (AM) and the finite element model (FEM) [Colour figure can be viewed at wileyonlinelibrary.com]

The actuator work is normalized to a longitudinal strain level of $\varepsilon_z = 1000\,\mu m\,m^{-1}$ at the trailing edge. Note that the actuator work neglects the compliance of any load-introducing structures such as load frames, beams, and adaptor plates.

The BJ-SCT concept is the most energy efficient concept using 32% of the energy required for a CF-SCT with the full cross section, whereas the CF-SCT with a cut cross- ection requires 55% of the energy required by the CF-SCT with a full cross section. In general, the CF-SCT concept requires more energy than the BJ-SCT since the bending stiffness contribution is larger in accordance with the parallel axis theorem (Equation 6).

TABLE 1 Actuator work

SCT concept	Work / 1000 μm m^{-1}	Rel. work
CF-SCT full	171 J	100%
CF-SCT	94 J	55%
BJ-SCT	55 J	32%

Abbreviations: BJ-SCT, ball joint subcomponent test; CF-SCT, C-frame subcomponent test; SCT, subcomponent test.

5 | CONCLUSIONS

Analytical models for simulating the structural performance of two different SCT concepts were derived and verified against FE results. Their predictions were found to be in good agreement with the numerical simulations. Thus, they can be implemented during a blade development phase to determine the optimal boundary conditions of an SCT, while simultaneously reducing the design and simulation effort. All SCTs show good agreement with the FST within a maximum deviation of 4% to 6% for the longitudinal strains. The maximum deviations of the transverse strains are in the range from 20% to 120% and the shear strains from 50% to 270%. All concepts are able to replicate the displacement field along the trailing edge and the out-of-plane deformation of the panels. The BJ-concept is in closer agreement with the FST because of the boundary conditions imposed. In contrast, the nodal rotations along the trailing edge can only be emulated by the BJ-SCT. The C-frame concepts constrain the rotational degree of freedom at the tip and root ends and therefore exhibit a discrepancy with respect to the FST. It is expected that the wavy shape of the rotational response is influenced by the specimen length, which will be investigated further.

When the method of subcomponent testing is projected onto a fatigue-loading scenario, the energy consumption is important. Taking the CF-SCT with full cross section to have an energy consumption of 100%, the cut cross section could potentially save 45%. Moreover, the lower bending stiffness with the BJ-SCT means the energy consumption could potentially be further reduced by up to 68% compared with those of the full cross section concepts. It should be noted that the deformation energy entering the load frames is not included and can increase the energy consumption depending on the load frame design.

ACKNOWLEDGEMENTS

This project is funded by the European Commission's Seventh Framework Programme as part of the IRPWind project (grant agreement No. 609795). We would like to thank SSP Technology A/S for providing the wind turbine blade model for this research.

AUTHOR CONTRIBUTIONS

M. Rosemeier derived the analytical models and carried out the finite element simulations. A. Antoniou initiated the joint publication and contributed with K. Branner and X. Chen to the introduction and interpretation of the results. P. Berring contributed to the determination of the analytical models and contributed together with F. Lahuerta to the finite element modeling.

ORCID

M. Rosemeier https://orcid.org/0000-0002-9853-0581
X. Chen https://orcid.org/0000-0001-6726-4068
F. Lahuerta https://orcid.org/0000-0001-9825-0232
K. Branner https://orcid.org/0000-0002-9601-6343

REFERENCES

1. IEC. *IEC 61400-23 - Wind Turbines Part 23: Full-scale Structural Testing of Rotor Blades*. Geneva, Switzerland: International Electrotechnical Commission.; 2012.
2. DNV GL AS. DNVGL-ST-0376 - rotor blades for wind turbines. https://rules.dnvgl.com/docs/pdf/DNVGL/ST/2015-12/DNVGL-ST-0376.pdf; 2015.
3. Rosemeier M., Basters G., Antoniou A. Benefits of subcomponent over full-scale blade testing elaborated on a trailing-edge bond line design validation. *Wind Energy Sci*. 2018;3(1):163-172.
4. IEC. *IEC 61400-5 - Wind Turbines Part 5: Wind Turbine Blades (Under Review)*. International Electrotechnical Commission; 2017.
5. Kühlmeier L. Buckling of wind turbine rotor blades: analysis, design and experimental validation. *Ph.D. Thesis*: Department of Mechanical Engineering, Aalborg University; 2007.
6. Berring P, Branner K, Berggreen C, Knudsen HW. Torsional performance of wind turbine blades-part 1: experimental investigation. In: 16th International Conference on Composite Materials; 2007; Kyoto, Japan. 8-13.

7. Branner K, Berring P, Berggreen C, Knudsen HW. Torsional performance of wind turbine blades–part ii: numerical validation. In: International Conference on Composite Materials (ICCM-16); 2007:8-13.
8. Ridzewski J. *Fatigue of Composite Materials and Structures*. Essen, Germany: Presentation at Haus der Technik; 2013.
9. Branner K, Berring P, Haselbach PU. Subcomponent testing of trailing edge panels in wind turbine blades. In: Proceedings of 17th European Conference on Composite Materials; 2016; Munich, Germany. 26-30.
10. Lahuerta F, de Ruiter MJ, Espinosa L, Koorn N, Smissaert D. Assessment of wind turbine blade trailing edge failure with sub-component tests. In: Proceedings of 21st International Conference on Composite Materials (ICCM21); 2017.
11. Rosemeier M, Bätge M, Antoniou A. A novel single actuator test setup for combined loading of wind turbine rotor blade sub-components. In: Proceedings of the 2nd International Symposium on Multiscale Experimental Mechanics: Multiscale Fatigue in Lyngby; 2017; Denmark.
12. Krimmer A, Leifheit R, Bardenhagen A. Assessment of quasi-static and fatigue performance of uni-directionally fibre reinforced polymers on the basis of matrix effort. In: Presented at 6th EASN International Conference on Innovation in European Aeronautics Research; 2016; Porto, Portugal.
13. Eder MA, Bitsche RD. Fracture analysis of adhesive joints in wind turbine blades. *Wind Energy*. 2015;18(6):1007-1022.
14. Eder MA, Bitsche RD, Nielsen M, Branner K. A practical approach to fracture analysis at the trailing edge of wind turbine rotor blades. *Wind Energy*. 2014;17(3):483-497.
15. Eder MA, Bitsche RD, Belloni F. Effects of geometric non-linearity on energy release rates in a realistic wind turbine blade cross section. *Compos Struct*. 2015;132:1075-1084.
16. Haselbach PU, Bitsche RD, Branner K. The effect of delaminations on local buckling in wind turbine blades. *Renew Energy*. 2016;85:295-305.
17. SSP Technology A/S. SSP 34 m data sheet; 2012.
18. Euler L. Methodus inveniendi lineas curvas maximi minimive propietate gaudentes, Additamentum I, De curvis elasticis; 1744.
19. Blasques JP, Stolpe M. Multi-material topology optimization of laminated composite beam cross sections. *Compos Struct*. 2012;94(11):3278-3289.
20. Blasques JP. Multi-material topology optimization of laminated composite beams with eigenfrequency constraints. *Compos Struct*. 2014;111:45-55.
21. Blasques JP, Bitsche RD. An efficient and accurate method for computation of energy release rates in beam structures with longitudinal cracks. *Eng Fract Mech*. 2015;133:56-69.
22. Blasques JP, Bitsche RD, Fedorov V, Lazarov BS. Accuracy of an efficient framework for structural analysis of wind turbine blades. *Wind Energy*. 2015;119(9):1603-1621.
23. Zahle F, Réthoré P-E, Graf P, Dykes K, Ning A. Fused-wind v0.1.0; 2015.
24. Gere JM, Goodno BJ. *Mechanics of Materials*, 8th ed. Florence, KY, USA: Cengage Learning, Inc; 2012.
25. Swanson JA. ANSYS Mechanical APDL. version 15.02014; 2014.
26. Branner K, Eder M, Berring P, et al. *Experimental Blade Research–Phase 2*. Denmark: DTU Wind Energy; 2015.
27. Rosemeier M, Berring P, Branner K. Non-linear ultimate strength and stability limit state analysis of a wind turbine blade. *Wind Energy*. 2016;19(5):825-846.
28. Thomsen CL, Eisenberg YP. *Blade test SSP34#2 Edgewise and Flapwise Final Static Test*. Denmark: Risø National Laboratory; 2003.
29. Bak C, Zahle F, Bitsche Robert, et al. Description of the DTU 10 MW reference wind turbine–DTU Wind Energy. Report-I-0092, Denmark, DTU Wind Energy; 2013.
30. Haselbach PU. An advanced structural trailing edge modelling method for wind turbine blades. *Compos Struct*. 2017;180:521-530.

How to cite this article: Rosemeier M, Antoniou A, Chen X, Lahuerta F, Berring P, Branner K. Trailing edge subcomponent testing for wind turbine blades–Part A: Comparison of concepts. *Wind Energy*. 2019;22:487–498. https://doi.org/10.1002/we.2301